

Magnon valley Hall effect in CrI₃-based vdW heterostructures

R. Hidalgo-Sacoto¹, R. I. Gonzalez², E. E. Vogel^{3,4}, S. Allende^{4,5}, José D. Mella^{4,6}, C. Cardenas^{4,6}, Roberto E. Troncoso⁷, and F. Muñoz^{4,6*}

¹*School of Physical Sciences and Nanotechnology, Yachay Tech, Urququí, Ecuador*

²*Centro de Nanotecnología Aplicada, Facultad de Ciencias, Universidad Mayor, Santiago, Chile*

³*Departamento de Ciencias Físicas, Universidad de La Frontera, Temuco, Chile, Chile*

⁴*Center for the Development of Nanoscience and Nanotechnology, CEDENNA, Santiago, Chile*

⁵*Departamento de Física, Universidad de Santiago de Chile, Santiago, Chile*

⁶*Departamento de Física, Facultad de Ciencias, Universidad de Chile, Santiago, Chile and*

⁷*Center for Quantum Spintronics, Department of Physics, Norwegian University of Science and Technology, NO-7491 Trondheim, Norway*

(Dated: February 3, 2020)

Magnonic excitations in the two-dimensional (2D) van der Waals (vdW) ferromagnet CrI₃ are studied. We find that bulk magnons exhibit a non-trivial topological band structure without the need for Dzyaloshinskii-Moriya (DM) interaction. This is shown in vdW heterostructures, consisting of single-layer CrI₃ on top of different 2D materials as MoTe₂, HfS₂ and WSe₂. We find numerically that the proposed substrates modify substantially the out-of-plane magnetic anisotropy on each sublattice of the CrI₃ subsystem. The induced staggered anisotropy, combined with a proper band inversion, leads to the opening of a topological gap of the magnon spectrum. Since the gap is opened non-symmetrically at the \mathbf{K}^+ and \mathbf{K}^- points of the Brillouin zone, an imbalance in the magnon population between these two valleys can be created under a driving force. This phenomenon is in close analogy to the so-called valley Hall effect (VHE), and thus termed as magnon valley Hall effect (MVHE). In linear response to a temperature gradient we quantify this effect by the evaluation of the temperature-dependence of the magnon thermal Hall effect. These findings open a different avenue by adding the valley degrees of freedom besides the spin, in the study of magnons.

I. INTRODUCTION

Magnons, the low-energy spin excitations of magnets, occupy a central place in the field of spintronics¹. Since magnons carry spin angular momentum and do possess electric charge, the understanding and control of their transport properties are of paramount importance^{2,3}. From a practical perspective, the lack of charge transport, implying the absence of loss of energy in the form of heat via Joule heating is certainly attractive.

Research on topological matter inspired a plethora of theoretical predictions of topological magnon systems during the last years. Among the first proposals showed that an engineered magnonic crystal develops topological bulk magnon bands and hence hosts chiral edge states⁴. Other alternative routes exploit mechanisms based on emergent gauge fields induced by magnetic textures, e.g., Skyrmion crystals^{5,6}. These magnetic phases provide a natural crystalline environment and shown that magnons inherit a topologically nontrivial band structure⁷⁻⁹. Interestingly, topological features are also present in certain lattice geometries like for instance, honeycomb¹⁰⁻¹³, Kitaev^{14,15} or Kagomé-lattice¹⁶⁻¹⁹ spin systems. In most of them the Dzyaloshinskii-Moriya (DMI) interaction is a key element^{10,20}, since it plays an analogous role to the spin-orbit coupling (SOC) in the Kane-Mele model²¹. However, theoretical studies have shown that magnonic bulk bands carry nontrivial Chern numbers, under the presence of nearest-neighbor pseudodipolar interaction²²⁻²⁴ and without the need for DMI.

In this work, we show that van der Waals (vdW) het-

erostructures, consisting of CrI₃ on top of different 2D materials with a hexagonal lattice open a topological gap in the magnon spectrum of the CrI₃ subsystem. Unlike previous schemes^{10,20}, based on the Dzyaloshinskii-Moriya coupling, our approach closely resembles that of an electrically-induced band gap in bilayer graphene²⁵⁻²⁷. The underlying mechanism that gives rise to this effect can be established by symmetry arguments. The honeycomb lattice of CrI₃ has a sublattice symmetry, with two identical but nonequivalent Cr atoms, see Fig. 1A. If we consider the heterostructure CrI₃|MX₂, being MX₂ the matched hexagonal material (e.g. a transition metal dichalcogenide), each Cr sublattice will have a different environment and thus, the sublattice symmetry is broken. Accordingly, the octahedrons of I atoms that wrap each Cr, are distorted differently for each sublattice. Therefore, the magnetocrystalline anisotropy energy will be different for each sublattice. It is worth commenting that this is independent of details such as the actual minimum energy configuration.

As a further step, we study the low-energy magnetic fluctuations of the effective spin system. We focus on magnonic excitations around the collinear ferromagnetic ground state, where the effects of the substrate appear as a staggered on-site energy added to the magnon Hamiltonian. Concretely, we construct the magnonic analogue of the valley Hall effect in graphene, breaking the inversion symmetry. In order to discuss the experimental accessibility of the predicted phenomena, we study magnon transport in linear response to a thermal bias. The non-trivial Berry curvature leads to the magnon thermal Hall effect, which is determined by the calculation of the

transverse thermal conductivity at finite temperature.

The paper is outlined as follows. In Sec. II we describe the numerical methods employed in this work. In Sec. III we first determine the most energetically favorable crystalline configuration between the CrI₃ layer and each of the proposed substrates. In Sec. IV we obtain all the relevant magnetic constants for the CrI₃ subsystem based on the previously derived magnetic Hamiltonian. The magnon valley Hall effect and its effects on the transverse thermal conductivity (via magnon thermal Hall effect) is computed. We conclude in Sec. V with a discussion of our results.

II. NUMERICAL METHODS

In this section we explained our approach for DFT calculations. We use the VASP package²⁸⁻³¹. The kinetic energy cutoff is set to 250 eV. The k-points grid is 11×11 . For the exchange-correlation term, we use the SCAN meta-GGA³² (actually SCAN+rVV10, see below). At least 12 Å of empty vacuum space is added to avoid spurious self-interactions along the non-periodic direction. To account for the Coulomb repulsion of Cr d-electrons, we use the DFT+U formulation³³ with parameters $U = 2.7$ eV and $J = 0.6$ eV³⁴; nevertheless, the value of magnetic constants is practically unaffected by these parameters (as long as the system remains insulating). The PyProcar code is employed for the analysis of eigenvalues.³⁵

To calculate the magnetocrystalline anisotropies, we use projector augmented-wave (PAW) pseudopotentials³⁶. The spin-orbit coupling is included in all calculations, including relaxations. The calculation of the individual anisotropy of each sublattice needs a non-collinear orientation of the magnetic moments around each Cr atom in order to explicitly break the sublattice symmetry (and hence have sublattice split anisotropies). This is possible by adding an extra penalty to the energy:

$$\Delta E_\epsilon = \epsilon \left[[\mathbf{m}_a - \hat{z}(\mathbf{m}_a \cdot \hat{z})]^2 + [\mathbf{m}_b - \hat{x}(\mathbf{m}_b \cdot \hat{x})]^2 \right], \quad (1)$$

with \mathbf{m}_α the magnetic moment around a Cr ion of the sublattice $\alpha = \{a, b\}$, *i.e.* $\mathbf{m}_\alpha = \int_{R_\alpha} \mathbf{m}(\mathbf{r}) d\mathbf{r}^3$, for some suitable radius R_α . The \hat{x}, \hat{z} axis refers to in-plane and out-of-plane directions. The parameter ϵ is a factor scaling the strength of the penalty. The energy from calculations with different values of ϵ cannot be directly compared. However, reversing the sublattice index in Eq. (1), provides a compatible equation to find the difference between the anisotropies of both sublattices. The penalty in the energy due to ϵ , can be decreased (in successive calculations) until it becomes much smaller than the anisotropy energies. Since the magnetic coupling of Cr ions is weak, the convergence of the magnetocrystalline energy with ϵ was almost immediate.

In a vdW system, it is crucial to have a good description of the dispersive forces. The SCAN+rVV10

approach³⁷, coupling the SCAN meta-GGA to the revised Vydrov and van Voorhis energy functional^{38,39} gives an accurate description of binding energies and lattice parameters of vdW materials⁴⁰. Our criterion for stopping the structural relaxation is 0.01 eV/Å as the largest force. Our electronic convergence criterion is 10^{-10} eV.

III. VDW HETEROSTRUCTURES AND SPIN HAMILTONIAN

In this section we review the CrI₃ lattice, we present the geometry of the proposed heterostructures, and how this translates in a Heisenberg-like Hamiltonian. The driving force behind the MVHE is the change of symmetry at the atomic level due to the heterostructure.

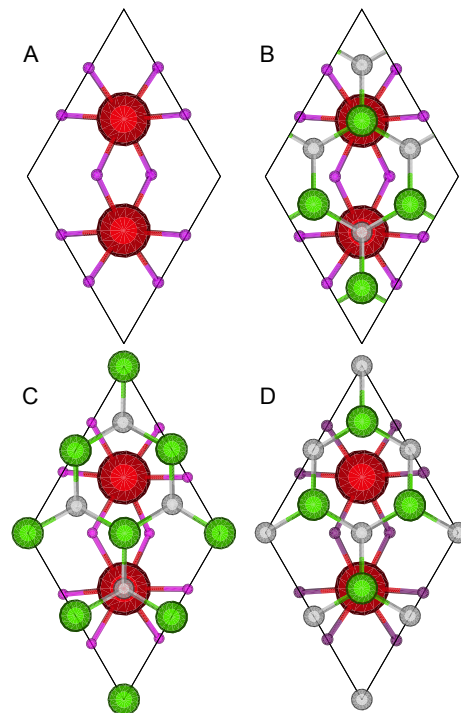


Figure 1. Top view of the unit cell of (A) CrI₃, Cr(I) atoms are the big red (small purple) spheres. (B-D) Different lateral arrangements of a heterostructure formed by a hexagonal lattice, on top of CrI₃. The medium-sized atoms belongs to different sublattices of the hexagonal system, white: metal (e.g. Mo, W, Hf), green: chalcogen (e.g. Te, Se, S).

CrI₃ has a honeycomb lattice, hence two identical sublattices formed by the Cr ions. Each Cr ion is surrounded by octahedron formed by six iodine atoms, see Fig. 1A. For the magnetic description (Heisenberg Hamiltonian) the iodine atoms can be ignored, they are non-magnetic. However, the consequences of altering the iodine octahedron will be present in the magnetic parameters. The lattice parameter of CrI₃ is $a = 6.95$ Å. If it forms a heterostructure with a two-dimensional (2D) hexagonal

system with a lattice parameter $a/2$, there is only one arrangement that preserves the sublattice symmetry of CrI_3 . However, most hexagonal 2D materials have at least two *different* sublattices (e.g. with different elements), and it is impossible to preserve the sublattice symmetry of CrI_3 in the composed system. The effects of this mechanism on the electronic structure of CrI_3 are small, it is a vdW interaction, but noticeable on their magnetic properties.

Among the materials whose lattice parameter is nearly $a/2$ we can name several transition metal dichalcogenides, with unit formula MX_2 (M is a transition metal and X a chalcogen atom) such as: MoTe_2 (3.5 Å), HfS_2 (3.6 Å), TiSe_2 (3.5 Å), WSe_2 (3.3 Å), WTe_2 (3.5 Å), etc. Other 2D materials also fit: GaS (3.6 Å), SnS_2 (3.6 Å). It may seem surprising that several 2D materials have a lattice parameter that is almost $a/2$. However, the bonding distance in several dichalcogenides ranges from 2.7 to 2.8 Å, which coincides with the Cr-I bonding distance, 2.75 Å. Another way to understand why the lattice parameter of CrI_3 practically doubles the value found in several hexagonal 2D materials is to consider a minimal hexagonal and a honeycomb lattices, ignoring all the atomic detail and only keeping the nodes. If the nodes in both lattices are at the same distance, the lattice parameter of the honeycomb is the double of the hexagonal lattice.

Table I. Relative binding energy, in meV/unit cell, of the different MX_2 systems on top of CrI_3 , see Fig. 1. The lowest energy arrangement for each system is taken as reference (*i.e.* 0 eV).

Arrangement	B	C	D
$\text{CrI}_3 \text{MoTe}_2$	4.8	43.5	0.0
$\text{CrI}_3 \text{HfS}_2$	18.0	108.9	0.0
$\text{CrI}_3 \text{WSe}_2$	19.9	65.8	0.0

In the following, we restrict our study to heterostructures of CrI_3 over MoTe_2 , HfS_2 and WSe_2 , in the three arrangements shown in Figs. 1B-D. Even though these materials have the same lattice and have a very similar composition (metal dichalcogenide), they produce different effects in the magnetic properties of CrI_3 . The relative energies among these arrangements, *i.e.*, taking the lowest energy conformation as reference, are given in Table I. In general, the most stable position is when a chalcogen atom is on top of a Cr atom, and the metals are in bridge positions (arrangement D). The spin Hamiltonian of these heterostructures is a slight variation of the one proposed by Lado and Fernández-Rossier³⁴:

$$H = - \sum_{i\alpha} D_\alpha (S_{i\alpha}^z)^2 - \sum_{\langle i\alpha, j\beta \rangle} \left[\frac{J}{2} \vec{S}_{i\alpha} \cdot \vec{S}_{j\beta} + \frac{\lambda}{2} S_{i\alpha}^z S_{j\beta}^z \right], \quad (2)$$

where \langle, \rangle stand for summation over next-nearest neighbors lattice sites. The indexes i, j run over each unit cell and α, β run over the sublattices $\{a, b\}$. The value

of the spin, $|\vec{S}_{i\alpha}|$, is $3/2$ ($3\mu_B$ per Cr atom). The first term is the magnetocrystalline anisotropy energy, with D_α depending only on the sublattice, a positive value of D_α implies an out-plane groundstate. The second term is a Heisenberg Hamiltonian, with J being the exchange constant ($J > 0$ for ferromagnetic interactions) and λ is the exchange anisotropy. According to Lado³⁴, λ is the main responsible for the magnetic order of CrI_3 . To find J, λ, D_a and D_b , we need to evaluate the energy of the FM and antiferromagnetic orders, oriented in-plane and out-plane. To get the actual value of D_a and D_b , we need to explicitly break the sublattice symmetry, by orientating one sublattice in-plane and the other out-plane (see Sec. II). Recently, other spin Hamiltonians have been proposed for modelling CrI_3 ^{41,42}, but the one we are using is particularly useful for DFT parameterization and to derive a low-energy magnon Hamiltonian.

The distortion due to the heterostructure also can induce different Cr-I-Cr paths, which in turn can induce a Dzyaloshinskii-Moriya coupling. We calculated the DM vector following the scheme used by Liu *et al.*⁴³ for the groundstate of the $\text{CrI}_3|\text{MoTe}_2$ heterostructure. As the geometry is similar for the other 2D materials, the order of magnitude found also should be similar. The values of D_z , the z -component of the DM vector, obtained in this way are smaller than 0.01 meV. Therefore, we will discard the contribution of the DMI to the magnetic Hamiltonian. Even in schemes specifically targeted to enhance DMI, its magnitude is often very small⁴⁴. Another source of DMI comes from the contributions of higher-order neighbors, which should be quite small due to the large interatomic distances. In bulk CrI_3 , with magnetic atoms breaking the inversion symmetry at neighbor layer, DMI can be large enough to be experimentally observed⁴⁵.

Table II. Magnetic constants of the different MX_2 systems on top of CrI_3 , in its groundstate arrangement. All the values are in meV, see Eq. 2

System	J	λ	D_a	D_b
CrI_3	2.20	0.11	0.04	0.04
$\text{CrI}_3 \text{MoTe}_2$	2.43	0.04	-0.18	0.33
$\text{CrI}_3 \text{HfS}_2$	2.05	0.13	-0.04	-0.07
$\text{CrI}_3 \text{WSe}_2$	2.32	0.04	0.04	0.07

The values of the magnetic constants, in the groundstate (atomic) configuration, are shown in Table II. The value of J varies only in about 10 %, since no fundamental change in the electronic structure happens. The anisotropy λ is much more affected, decreasing to half its value in $\text{CrI}_3|\text{MoTe}_2$ and $\text{CrI}_3|\text{WSe}_2$. This is explained by the distortion on CrI_3 once in contact with another material, for instance, both Cr sublattices no longer are co-planar. Nevertheless, the value of λ remains positive, indicating a FM easy axis. Finally, the magnetocrystalline anisotropy suffers strong variations, especially in MoTe_2 . The strong variations in the anisotropy constants can be expected: alterations of the symmetry of the lo-

cal environment (even in vdW systems) can induce large changes, even inducing an easy axis⁴⁶. In some of the heterostructures studied, the change of D_α also includes a change of its sign ($D_\alpha < 0$), this does not mean a change of easy axis, since the exchange anisotropy λ dominates and is positive in every heterostructure.

IV. MAGNON VALLEY HALL EFFECT

In this section we study spin fluctuations in the limit of small deviations (magnons) around the equilibrium state. We consider the ground state to be collinear and parallel to the z -direction. Magnonic excitations are introduced by the standard Holstein-Primakoff⁴⁷ transformation that quantizes the spins in terms of bosons⁴⁸.

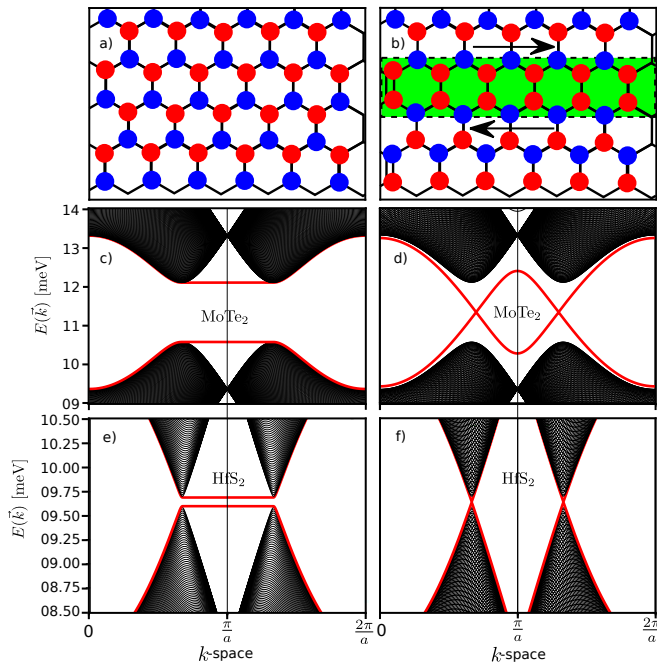


Figure 2. (a) Bulk honeycomb lattice formed by the Cr atoms, different onsite terms in Eq. 3 are marked by different colors. (b) A 1D domain wall swapping the sublattices (*i.e.*, the onsite term in the spin Hamiltonian), the topologically protected magnon states will appear around this region. Magnon edge states (red lines) and subbands (black lines) of a finite ribbon of CrI₃|MoTe₂ and CrI₃|HfS₂ without (c, e) and with (d, f) a domain wall. With the domain wall, the topological edge states bridge the gap in both cases.

The spin Hamiltonian given by Eq. (2) can be expanded up to second order in magnon operators resulting in $H = H_0 + H_m$. The zero-point energy is represented by H_0 , while the nearest neighbor tight-binding Hamiltonian for the magnonic excitations is $H_m = -\frac{JS}{2} \sum_{\langle i,j \rangle} (d_i^\dagger d_j + h.c) + \Omega \sum_i d_i^\dagger d_i$, in the absence of substrates and where $\Omega = S(2D+3(J+\lambda))$. The magnon operator d_i (d_i^\dagger) corresponds to the annihilation (creation) operator at the i -th site. The Hamiltonian

H_m is similar to the electronic Hamiltonian of graphene, with two Dirac points existing at $\mathbf{K}^+ = (2\pi/\sqrt{3}a, 0)$ and $\mathbf{K}^- = (-2\pi/\sqrt{3}a, 0)$ in the Brillouin zone. In CrI₃, a magnon gap $\Delta_0 = 3S\lambda = 0.4$ meV for the lower energy band and critical temperature of $T_c = 85$ K are found³⁴. Under the presence of the proposed substrates, the Cr environment changes within the unit cell, thus modifying the magnetocrystalline anisotropy energy in each sublattice. The effect on the Hamiltonian H_m is readily captured by mapping the magnon operators into the sublattice-magnon basis,

$$H_m = -JS \sum_{\langle i,j \rangle} (a_i^\dagger b_j + h.c) + \Omega_a \sum_i a_i^\dagger a_i + \Omega_b \sum_i b_i^\dagger b_i, \quad (3)$$

where a^\dagger and b^\dagger represent magnon creation operators on the sublattices a and b , respectively. Also, we defined $\Omega_\alpha = [2D_\alpha S + 3S(J+\lambda)]$. The induced effect by substrates on the magnon bands can be readily captured in the momentum representation. In Fourier space the magnon Hamiltonian then reads $H_m = \sum_{\mathbf{k}} \Psi_{\mathbf{k}}^\dagger [\Delta \mathbb{I} + \mathbf{h}_{\mathbf{k}} \cdot \boldsymbol{\tau}] \Psi_{\mathbf{k}}$, with $\Psi_{\mathbf{k}} = (a_{\mathbf{k}}, b_{\mathbf{k}})$ the spinor of Fourier transformed operators and $\boldsymbol{\tau}$ the Pauli matrix vector. The field $\mathbf{h}_{\mathbf{k}} = \sum_j (-JS \cos(\mathbf{k} \cdot \mathbf{v}_j), JS \sin(\mathbf{k} \cdot \mathbf{u}_j), \Delta)$, with $\bar{\Delta} = (\Omega_a + \Omega_b)/2$ and $\Delta = (\Omega_a - \Omega_b)/2$. The eigenenergies for the upper and lower magnon bands are given by $\epsilon_{\mathbf{k}}^\pm = \bar{\Delta} \pm |\mathbf{h}_{\mathbf{k}}|$. In the limit $\Omega_a = \Omega_b$ both bands become degenerated at the Dirac points \mathbf{K}^+ and \mathbf{K}^- , with a Dirac-type dispersion around these points. In the presence of the substrates, the magnetic anisotropy becomes different on each sublattice and a band-gap is open at \mathbf{K}^+ (\mathbf{K}^-) with value 2Δ . It is worth noticing that the gaps open differently since $\epsilon_{\pm}^{\mathbf{K}^+} = \bar{\Delta} \pm \Delta$ and $\epsilon_{\pm}^{\mathbf{K}^-} = \bar{\Delta} \mp \Delta$. The Berry curvatures of the upper and the lower magnon bands are largely concentrated, and opposites in sign, around the corners of the BZ⁴⁹. Thus, the Chern number of each band is zero²⁴. However, restricting the integration zone to a single valley, around \mathbf{K}^+ , the Chern number is $c_n^\pm = \int \Omega_z^\pm dk^2 = \pm 1$ ⁴⁹.

Although perpendicularly magnetized honeycomb lattices with staggered anisotropy on each sublattices are topologically trivial, this represents the basic ingredient to induce a magnon valley Hall effect in a CrI₃-based vdW heterostructure. Motivated by related works on graphene-like structures⁵⁰, we consider an induced *band inversion* as a second ingredient. This consists in a sign change of the bandgap obtained, *e.g.*, swapping the sublattices $a \leftrightarrow b$, that in turn implies swapping the anisotropy $D_a \leftrightarrow D_b$. The last can be achieved by inducing a line defect on the MX₂ monolayer, see Fig. 2b. This type of defect has been extensively studied, being the most common methods to induce this inversion those based on chalcogen defects⁵¹⁻⁵³, see Ref. [54] and references therein. Recently, a sublattice inversion induced by irradiation has been reported for MoTe₂.⁵⁵ Another method to create a post-synthesis sublattice inversion is by means of the incorporation of excess Mo

atoms in MoTe₂. This induces self-organization into highly-ordered 1D patterns that reach a length of several nanometers.⁵⁶

In Figs. 2c and 2e we show, in a zigzag nanoribbon without line defect, that the edges states are flat bands connecting the \mathbf{K}^+ and \mathbf{K}^- valleys. The bandgap achieved by this vdW heterostructure goes from 0.1 meV (CrI₃|HfS₂) to nearly 1.5 meV (CrI₃|MoTe₂). Depending on the actual nanoribbon termination, extra edges states can appear (due to non-bonding atoms in the chemical jargon)⁵⁷.

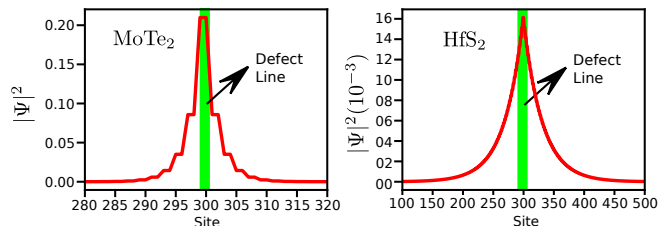


Figure 3. Topological protected states wavefunction at defect line near projection of \mathbf{K}^+ point, left panel show CrI₃|MoTe₂ wavefunction (large band-gap) and right panel CrI₃|HfS₂ wavefunction (small band-gap). The localization length is much larger for systems with smaller magnon bandgap.

When sublattice inversion is considered by introducing a line defect (Fig. 2b) and the condition $J/4 \geq |D_a - D_b|$ is fulfilled, the magnon valley hall effect (MVHE) is presented in the system. Two topologically protected states with opposite velocities at the defect line appear connecting the valence and conduction bands (Fig. 2d,f). Particularly, CrI₃ with all substrates meet the necessary condition to exhibit this effect. These states at the defect line (see Fig. 3) have an exponential decay that depends on the band-gap induced by the substrate without defect line. While the topological states are localized, its penetration depth is strongly dependent of the topological bandgap. The localization of these states have deep consequences in presence of disorder braking the sublattice symmetry (*i.e.* disorder in anisotropies). When the edge state penetrates several sites, the atomic disorder averages to zero, making the edge state mostly unaffected even in the case of disorder-induced bandgap, even for very large values of the disorder⁵⁸.

In order to connect the MVHE with experimentally accessible measurements, we consider magnon transport in the vdW heterostructures in presence of a thermal bias. In linear response, we compute the magnon thermal Hall conductivity, κ_{xy} ⁵⁹, under a longitudinal temperature gradient. Following standard transport theory, we compute the thermal conductivity given by the expression, $\kappa_{xy} = -k_B^2 T / h^2 \sum_{n=\pm} \int (c_2(g(\epsilon_{nk})) - \pi^2/3) \Omega_z^n(k) d\mathbf{k}$, where the sum runs over both eigenvalues, ϵ_{\pm} , and $g(\epsilon)$ is the Bose-Einstein distribution. The function c_2 ⁶⁰ is a monotonous function satisfying $c_2(0) \rightarrow 0$ and $c_2(\infty) \rightarrow \pi^2/3$. The value of κ_{xy} integrated over all the Brillouin zone is exactly zero, since both valleys have an opposite

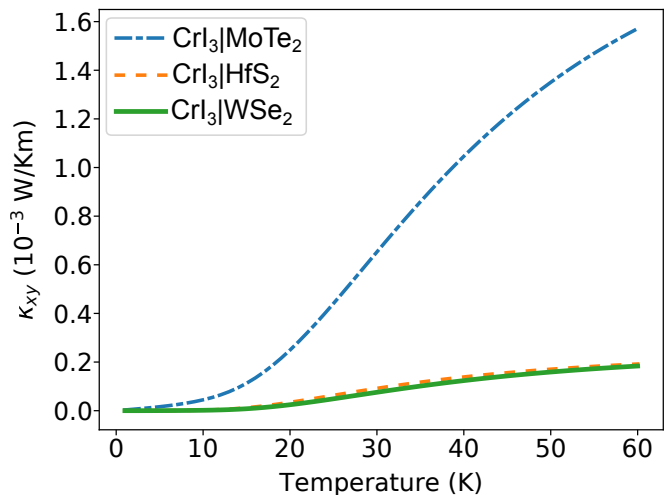


Figure 4. Temperature-dependent magnon thermal Hall conductivity κ_{xy} for each of the proposed vdW heterostructures. A thickness of 1 nm was used to normalize κ_{xy} . The temperature range is intentionally considered up to the critical temperature $T_C = 85\text{K}$.

Berry curvature. If we restrict the integral to a neighborhood around \mathbf{K}^+ , we will get the contribution of each valley to the Hall thermal conductivity. The valley effect of magnons arises when a defect line swaps both sublattices, following the mechanism introduced above. In Fig. 4 we show the temperature-dependent thermal conductivity. The result of κ_{xy} for every vdW heterostructure is in the range of 10^{-3} (W/Km), close to the thermal conductivity of other topological schemes⁵⁹. Importantly, when the temperature increases we see a significant upturn of κ_{xy} for CrI₃|MoTe₂, contrary to the other heterostructures due to their small gap. As is expected, the thermal conductivity reaches a maximum value, roughly at a similar critical temperature, then decay to zero for larger temperature.

V. CONCLUSIONS

In this paper, we proposed a mechanism to induce topologically non-trivial states in the magnon spectrum of a single layer of CrI₃, in analogy with the valley Hall effect in the electronic structure of bilayer graphene. The topological edge states are achieved when (*i*) each sublattice has a different magnetocrystalline anisotropy and (*ii*) there exists a region where the magnetocrystalline of both sublattices swaps. A sublattice-dependent magnetocrystalline anisotropy, is obtained by forming a vdW heterostructure with another (non-magnetic) hexagonal 2D material or substrate. The local sublattice inversion requires a line defect in the CrI₃ layer. These defects, with an extension of several nanometers, can be found naturally or artificially induced with great accuracy. We quantified this effect by DFT calculations of the heterostructures of CrI₃ with MoTe₂, HfS₂ and WSe₂. The

topological bandgap induced in the magnon spectrum in the previous materials ranged between 0.1 to 1.5 meV. Finally, we show that the MVHE manifests itself in the form of a magnon thermal Hall effect, due to the non-trivial topology of the band structure, when a thermal gradient is applied along the heterostructure. This effect is quantified by the evaluation of the temperature-dependent transverse thermal conductivity.

ACKNOWLEDGMENTS

This work was partially funded by Fondecyt grants 1190036 (EEV), 1191353 (FM), 11180557 (RIG), Conicyt doctoral fellowship grants 21151207 (JM), the Center for the Development of Nanoscience and Nanotechnology CEDENNA FB-0807, the supercomputing infrastructure of the NLHPC (ECM-02) and from Conicyt PIA/Anillo ACT192023 (FM). R.E.T acknowledges the support by the European Union's Horizon 2020 Research and Innovation Programme under Grant DLV-737038 "TRANSPIRE" and the Research Council of Norway through its Centres of Excellence funding scheme, Project No. 262633, "QuSpin". The authors thank fruitful discussion with Luis E. F. Foa Torres.

-
- * fvmunoz@gmail.com
- ¹ A. V. Chumak, V. I. Vasyuchka, A. A. Serga, and B. Hillebrands, *Nature Physics* **11**, 453 (2015).
 - ² V. V. Kruglyak, S. O. Demokritov, and D. Grundler, *Journal of Physics D: Applied Physics* **43**, 264001 (2010).
 - ³ A. A. Serga, A. V. Chumak, and B. Hillebrands, *Journal of Physics D: Applied Physics* **43**, 264002 (2010).
 - ⁴ R. Shindou, R. Matsumoto, S. Murakami, and J.-i. Ohe, *Phys. Rev. B* **87**, 174427 (2013).
 - ⁵ N. Nagaosa and Y. Tokura, *Nature Nanotechnology* **8**, 899 (2013).
 - ⁶ A. Fert, N. Reyren, and V. Cros, *Nature Reviews Materials* **2**, 17031 (2017).
 - ⁷ T. Schwarze, J. Waizner, M. Garst, A. Bauer, I. Stasinopoulos, H. Berger, C. Pfeleiderer, and D. Grundler, *Nature Materials* **14**, 478 (2015).
 - ⁸ A. Roldn-Molina, A. S. Nunez, and J. Fernández-Rossier, *New Journal of Physics* **18**, 045015 (2016).
 - ⁹ M. Garst, J. Waizner, and D. Grundler, *Journal of Physics D: Applied Physics* **50**, 293002 (2017).
 - ¹⁰ S. K. Kim, H. Ochoa, R. Zarzuela, and Y. Tserkovnyak, *Phys. Rev. Lett.* **117**, 227201 (2016).
 - ¹¹ S. A. Owerre, *Journal of Physics: Condensed Matter* **28**, 386001 (2016).
 - ¹² R. Cheng, S. Okamoto, and D. Xiao, *Phys. Rev. Lett.* **117**, 217202 (2016).
 - ¹³ V. A. Zyuzin and A. A. Kovalev, *Phys. Rev. Lett.* **117**, 217203 (2016).
 - ¹⁴ P. A. McClarty, X.-Y. Dong, M. Gohlke, J. G. Rau, F. Pollmann, R. Moessner, and K. Penc, *Phys. Rev. B* **98**, 060404 (2018).
 - ¹⁵ D. G. Joshi, *Phys. Rev. B* **98**, 060405 (2018).
 - ¹⁶ R. Chisnell, J. S. Helton, D. E. Freedman, D. K. Singh, R. I. Bewley, D. G. Nocera, and Y. S. Lee, *Phys. Rev. Lett.* **115**, 147201 (2015).
 - ¹⁷ R. Seshadri and D. Sen, *Phys. Rev. B* **97**, 134411 (2018).
 - ¹⁸ S. A. Owerre, *Journal of Physics: Condensed Matter* **30**, 245803 (2018).
 - ¹⁹ D. Malz, J. Knolle, and A. Nunnenkamp, *Nature Communications* **10** (2019), 10.1038/s41467-019-11914-2.
 - ²⁰ L. Zhang, J. Ren, J.-S. Wang, and B. Li, *Phys. Rev. B* **87**, 144101 (2013).
 - ²¹ C. L. Kane and E. J. Mele, *Phys. Rev. Lett.* **95**, 226801 (2005).
 - ²² X. S. Wang, Y. Su, and X. R. Wang, *Phys. Rev. B* **95**, 014435 (2017).
 - ²³ X. S. Wang, H. W. Zhang, and X. R. Wang, *Phys. Rev. Applied* **9**, 024029 (2018).
 - ²⁴ X. S. Wang and X. R. Wang, *Journal of Physics D: Applied Physics* **51**, 194001 (2018).
 - ²⁵ F. Munoz, H. P. O. Collado, G. Usaj, J. O. Sofo, and C. A. Balseiro, *Phys. Rev. B* **93**, 235443 (2016).
 - ²⁶ E. McCann and M. Koshino, *Reports on Progress in Physics* **76**, 056503 (2013).
 - ²⁷ L. Ju, Z. Shi, N. Nair, Y. Lv, C. Jin, J. Velasco Jr, C. Ojeda-Aristizabal, H. A. Bechtel, M. C. Martin, A. Zettl, *et al.*, *Nature* **520**, 650 (2015).
 - ²⁸ G. Kresse and J. Hafner, *Phys. Rev. B* **47**, 558 (1993).
 - ²⁹ G. Kresse and J. Hafner, *Phys. Rev. B* **49**, 14251 (1994).
 - ³⁰ G. Kresse and J. Furthmüller, *Comput. Mater. Sci.* **6**, 15 (1996).
 - ³¹ G. Kresse and J. Furthmüller, *Phys. Rev. B* **54**, 11169 (1996).
 - ³² J. Sun, A. Ruzsinszky, and J. P. Perdew, *Phys. Rev. Lett.* **115**, 036402 (2015).
 - ³³ A. I. Liechtenstein, V. I. Anisimov, and J. Zaanen, *Phys. Rev. B* **52**, R5467 (1995).
 - ³⁴ J. L. Lado and J. Fernández-Rossier, *2D Materials* **4**, 035002 (2017).
 - ³⁵ U. Herath, P. Tavazde, X. He, E. Bousquet, S. Singh, F. Muñoz, and A. H. Romero, *Computer Physics Communications*, 107080 (2019).
 - ³⁶ G. Kresse and D. Joubert, *Phys. Rev. B* **59**, 1758 (1999).
 - ³⁷ H. Peng, Z.-H. Yang, J. P. Perdew, and J. Sun, *Phys. Rev. X* **6**, 041005 (2016).
 - ³⁸ R. Sabatini, T. Gorni, and S. de Gironcoli, *Phys. Rev. B* **87**, 041108 (2013).
 - ³⁹ O. A. Vydrov and T. Van Voorhis, *The Journal of Chemical Physics* **133**, 244103 (2010).
 - ⁴⁰ S. A. Tawfik, T. Gould, C. Stampfl, and M. J. Ford, *Phys. Rev. Materials* **2**, 034005 (2018).
 - ⁴¹ I. V. Kashin, V. V. Mazurenko, M. I. Katsnelson, and A. N. Rudenko, "Orbitally-resolved ferromagnetism of monolayer CrI_3 ," (2019), [arXiv:1912.11828](https://arxiv.org/abs/1912.11828) [cond-mat.str-el].

- ⁴² I. Lee, F. G. Utermohlen, D. Weber, K. Hwang, C. Zhang, J. van Tol, J. E. Goldberger, N. Trivedi, and P. C. Hammel, *Phys. Rev. Lett.* **124**, 017201 (2020).
- ⁴³ J. Liu, M. Shi, J. Lu, and M. P. Anantram, *Phys. Rev. B* **97**, 054416 (2018).
- ⁴⁴ S. Ghosh, N. Stoji, and N. Binggeli, *Physica B: Condensed Matter* **570**, 166 (2019).
- ⁴⁵ L. Chen, J.-H. Chung, B. Gao, T. Chen, M. B. Stone, A. I. Kolesnikov, Q. Huang, and P. Dai, *Phys. Rev. X* **8**, 041028 (2018).
- ⁴⁶ F. Muñoz, J. Mejía-López, T. Pérez-Acle, and A. H. Romero, *ACS Nano* **4**, 2883 (2010).
- ⁴⁷ T. Holstein and H. Primakoff, *Phys. Rev.* **58**, 1098 (1940).
- ⁴⁸ The Holstein-Primakoff transformation is defined by $S_i^+ = \sqrt{2S - d_i^\dagger d_i} d_i$, $S_i^- = d_i^\dagger \sqrt{2S - d_i^\dagger d_i}$ and $S_i^z = (S - d_i^\dagger d_i)$ with S the spin quantum number. One magnon, created (annihilated) at site i of the lattice by the operator d_i^\dagger (d_i), corresponds to changing the total spin with $+\hbar$ ($-\hbar$).
- ⁴⁹ The Berry curvature of each band is calculated from, $\Omega^\pm = \mp \hat{\mathbf{h}} \cdot (\partial_{k_x} \hat{\mathbf{h}} \times \partial_{k_y} \hat{\mathbf{h}}) / 2$. Expanding around \mathbf{K}^+ , the only non-zero components of the Berry curvature are, $\Omega_z^\pm = \pm \frac{3}{4} (aJS)^2 \Delta (3(aJS)^2 (q_x^2 + q_y^2) / 4 + \Delta^2)^{-3/2}$. The Chern number, c_n , is the integral of the Berry curvature along the Brillouin zone, which is zero, because the contributions around each valley cancels. However, if we restrict the integration zone to a single valley only, let say close to \mathbf{K}^+ , we can calculate its Chern number, $c_n^\pm = \int \Omega_z^\pm dk^2 = \pm 1$.
- ⁵⁰ W. Yao, S. A. Yang, and Q. Niu, *Phys. Rev. Lett.* **102**, 096801 (2009).
- ⁵¹ C. J. Alvarez, M. T. Dau, A. Marty, C. Vergnaud, H. L. Poche, P. Pochet, M. Jamet, and H. Okuno, *Nanotechnology* **29**, 425706 (2018).
- ⁵² M. Schleberger and J. Kotakoski, *Materials* **11**, 1885 (2018).
- ⁵³ H.-P. Komsa, S. Kurasch, O. Lehtinen, U. Kaiser, and A. V. Krasheninnikov, *Phys. Rev. B* **88**, 035301 (2013).
- ⁵⁴ M. Batzill, *Journal of Physics: Condensed Matter* **30**, 493001 (2018).
- ⁵⁵ K. Elibol, T. Susi, G. Argentero, M. Reza Ahmadpour Monazam, T. J. Pennycook, J. C. Meyer, and J. Kotakoski, *Chemistry of Materials* **30**, 1230 (2018).
- ⁵⁶ P. M. Coelho, H.-P. Komsa, H. Coy Diaz, Y. Ma, A. V. Krasheninnikov, and M. Batzill, *ACS Nano* **12**, 3975 (2018).
- ⁵⁷ J. Li, I. Martin, M. Bttiker, and A. F. Morpurgo, *Physica Scripta* **T146**, 014021 (2012).
- ⁵⁸ F. Munoz, F. Pinilla, J. Mella, and M. I. Molina, *Scientific reports* **8**, 1 (2018).
- ⁵⁹ P. Laurell and G. A. Fiete, *Phys. Rev. B* **98**, 094419 (2018).
- ⁶⁰ The function c_2 is defined as, $c_2(x) = (1+x) \left[\ln \left(\frac{1+x}{x} \right) \right]^2 - (\ln(x))^2 - 2\text{Li}_2(-x)$, where Li_n is the polylogarithm function.